

# Large-Eddy Simulation Study of Log Laws in a Neutral Ekman Boundary Layer

QINGFANG JIANG AND SHOUPING WANG

*Naval Research Laboratory, Monterey, California*

PETER SULLIVAN

*National Center for Atmospheric Research, Boulder, Colorado*

(Manuscript received 22 May 2017, in final form 9 February 2018)

## ABSTRACT

The characteristics of wind profiles in a neutral atmospheric boundary layer and their dependence on the geostrophic wind speed  $U_g$ , Coriolis parameter  $f$ , and surface roughness length  $z_0$  are examined utilizing large-eddy simulations. These simulations produce a constant momentum flux layer and a log-law layer above the surface characterized by a logarithmic increase of wind speed with height. The von Kármán constant derived from the mean wind profile is around 0.4 over a wide range of control parameters. The depths of the simulated boundary layer, constant-flux layer, and surface log-law layer tend to increase with the wind speed and decrease with an increasing Coriolis parameter. Immediately above the surface log-law layer, a second log-law layer has been identified from these simulations. The depth of this upper log-law layer is comparable to its counterpart in the surface layer, and the wind speed can be scaled as  $u_* (u_* / fh)^{3/4}$ , as opposed to just  $u_*$  in the surface log-law layer, implying that in addition to surface processes, the upper log-law layer is also influenced by Earth's rotation and large-scale conditions. Here  $u_*$  is the friction velocity at the surface, and  $h$  is the boundary layer depth. An analytical model is proposed to assist in the interpretation of the log laws in a typical Ekman boundary layer. The physics and implications of the upper log-law layer are discussed.

## 1. Introduction


In a neutral atmospheric Ekman boundary layer, there exists a log-law layer above the surface in which the mean horizontal wind speed increases logarithmically with the vertical distance from the surface, namely,

$$\frac{U}{u_*} = \frac{1}{\kappa} \log \left( \frac{z}{z_0} \right), \quad (1)$$

where  $U$  is the mean horizontal wind component in the surface stress direction (or wind speed),  $z$  is the vertical distance from the surface,  $z_0$  is the surface roughness length,  $u_* = \sqrt{\tau_0 / \rho_0}$  is the surface friction velocity,  $\tau_0$  is the surface stress,  $\rho_0$  is the air density, and  $\kappa = 0.4$  is the von Kármán constant. The so-called log law or law of the wall

for pipe flow and channel flow was first proposed by Prandtl (1925) based on the mixing-length concept, later by von Kármán (1930) through similarity theory, by Millikan (1938) through asymptotic matching, by Buschmann and Gad-el Hak (2007) based on dimensional analysis, and by George and Castillo (1997) through asymptotic analysis of high-Reynolds number flows. In a seminal paper, Monin and Obukhov (1954) generalized the mixing-length theory and log law for a neutral surface layer to stable and convective conditions by hypothesizing that mean profiles of wind speed, temperature, and other scalars in the surface layer, when properly normalized, are universal functions of the dimensionless height (i.e.,  $z$  normalized by the Obukhov length, a stability-based length scale). This theory, later known as Monin–Obukhov similarity theory, is generally supported by field observations over a homogeneous land surface (e.g., Businger et al. 1971) and is widely recognized as a cornerstone of modern micrometeorology (e.g., Foken 2006).

For a steady atmospheric Ekman boundary layer (EBL), the equations of motion can be written as (e.g., Tennekes 1973),

 Denotes content that is immediately available upon publication as open access.

Corresponding author: Qingfang Jiang, qingfang.jiang@nrlmry.navy.mil

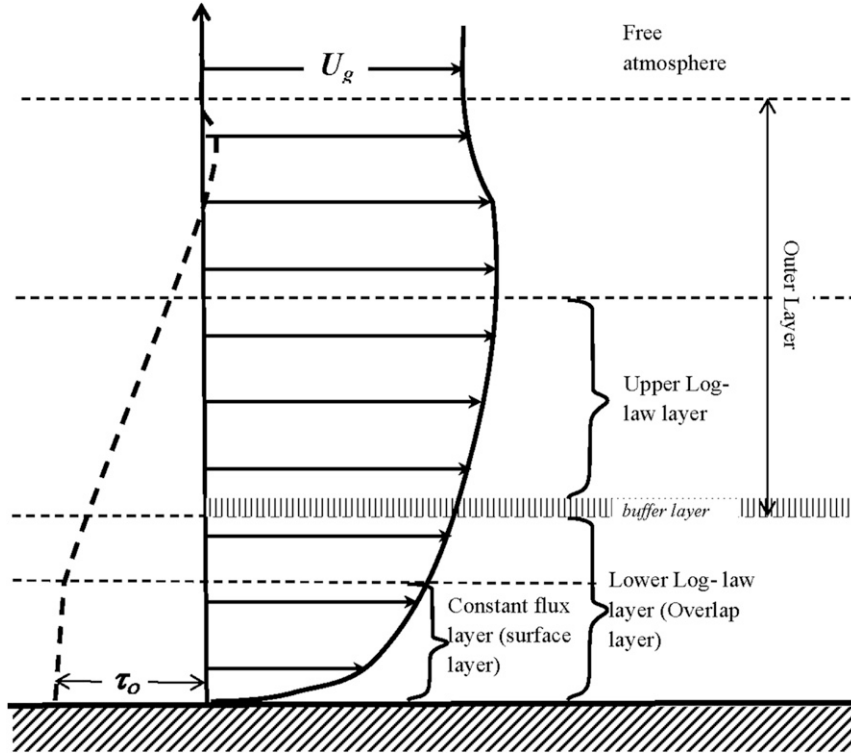


FIG. 1. Schematics of the atmospheric Ekman BL structure. The bold curves correspond to the horizontal wind speed (solid) and momentum flux profiles (dashed). The lower and upper log-law layers are separated by a thin buffer layer. The constant-flux layer is located above the surface and is shallower than the lower log-law layer.

$$-f(V - V_g) = \frac{d}{dz}(-\overline{u'w'}) \quad \text{and} \quad (2)$$

$$f(U - U_g) = \frac{d}{dz}(-\overline{v'w'}), \quad (3)$$

$$\frac{U - U_g}{u_*} = F_x\left(\frac{fz}{u_*}\right) \quad \text{and} \quad (5)$$

$$\frac{V - V_g}{u_*} = F_y\left(\frac{fz}{u_*}\right), \quad (6)$$

where  $U$  and  $V$  are the mean horizontal wind components,  $U_g$  and  $V_g$  are the corresponding geostrophic wind components,  $f$  is the Coriolis parameter,  $(u', v', w')$  represent the turbulent wind components, and  $(\overline{u'w'}, \overline{v'w'})$  denote the vertical fluxes of the horizontal momentum components. The only external nondimensional parameter for this system is the surface Rossby number  $R_o = G/(fz_0)$ , where  $G = \sqrt{U_g^2 + V_g^2}$  is the geostrophic wind speed. According to Blackadar and Tennekes (1968) and Tennekes (1973), in an atmospheric boundary layer (ABL),  $R_o \rightarrow \infty$ , and the system [(2) and (3)] admits two self-similar solutions (often referred to as Rossby similarity). Near the surface  $fz/u_* \rightarrow 0$ , and to the first order of approximation, one obtains

$$\frac{U}{u_*} = F_s\left(\frac{z}{z_0}\right) \quad \text{and} \quad \frac{V}{u_*} = 0, \quad (4)$$

and in the outer layer, where  $z/z_0 \rightarrow \infty$ , the wind profile can be asymptotically written as

where  $F_s$  and  $(F_x, F_y)$  denote well-behaved universal functions of the nondimensional altitude  $z/z_0$  and  $fz/u_*$ , respectively. Solution (4) suggests that the momentum flux is asymptotically constant in the surface layer (Blackadar and Tennekes 1968; Wyngaard 2010), which is also referred to as the constant-flux (CFLX) layer (Fig. 1). Tennekes (1973) suggests that the log law is valid in both the surface (i.e., constant flux) layer and beyond. The log-law layer is also referred to as a matching layer, overlap layer, or inertial sublayer (Blackadar and Tennekes 1968). However, their analysis cannot provide an upper limit for the vertical extent of the constant-flux layer or the log-law layer. Nevertheless, both the constant-flux and log-law layers in the atmospheric EBL have been documented by numerous field observations. The observed log-law layers in a neutral atmosphere range from dozens of meters to more than a 100 m. For example, observations of wind

speed over homogenous surfaces under small–Richardson number (i.e., nearly neutral) conditions by [Carl et al. \(1973; 150-m tower\)](#) found no significant deviations from logarithmic profiles up to 150 m. Similarly, [Horiguchi et al. \(2012; 213-m tower\)](#) found that under neutral conditions and with an average wind speed of  $12.2 \text{ m s}^{-1}$  aloft, the observed wind speed increases with height logarithmically up to 150 m above the ground. Over the past three decades, the log-law layer has been reproduced numerically using direct numerical simulation (DNS) or large-eddy simulation (LES) codes. In DNS studies, the Reynolds number ( $Re$ ) is usually substantially smaller than that for a typical atmospheric boundary layer flow ( $Re \sim 10^5$ – $10^{10}$ ) as a result of the limitation in computing power [e.g.,  $Re$  is equal to 1000 in [Coleman \(1999\)](#) and 5200 in [Lee and Moser \(2015\)](#)]. LES codes have problems resolving processes near the ground surface, where the scale of dominant eddies, comparable to the vertical distance from the surface, becomes too small to be well resolved. The LES-simulated mean winds tend to deviate from the well-established log-law profile near the surface as a result of the imperfection of subgrid-scale (SGS) models, a problem known as “overshoot” or “mismatch” ([Mason and Thomson 1992](#)). This was especially a problem historically, when the LES model resolutions were much coarser. For example, [Cai and Steyn \(1996\)](#) find that their simulated von Kármán constant  $\kappa_{LES}$  is dependent on the “Smagorinsky-Model Reynolds number,” which is a function of the model grid spacings, instead of a universal constant. With horizontal grid spacings between 20 and 60 m, the largest  $\kappa_{LES}$  they obtained is 0.35, which is substantially smaller than the widely accepted value of 0.4. In the past 25 years, this issue has been addressed by several studies using different SGS models (e.g., [Sullivan et al. 1994](#); [Wyngaard et al. 1998](#); [Chow et al. 2005](#); [Brasseur and Wei 2010](#); [Stoll and Porté-Agel 2006](#); [Kawai and Larsson 2012](#)).

Solutions (5) and (6), also known as the velocity defect law, are valid for the outer Ekman layer. The vertical variation of the horizontal winds in an Ekman layer can also be obtained by analytically or numerically solving (2) and (3) with additional assumptions about the momentum fluxes. For example, in  $K$  theory, the momentum fluxes are assumed to be proportional to the vertical gradient of the mean wind components, that is,  $(-\overline{u'w'}, -\overline{v'w'}) = K_m(dU/dz, dV/dz)$ , where the eddy viscosity  $K_m$  is constant with height or is an analytical function of  $z$  ([Holton 1992](#)). In addition, the characteristics of an EBL have been examined in a laboratory (e.g., [Howroyd and Slawson 1975](#)) and numerically using LES or DNS codes ([Coleman et al. 1990](#); [Zikanov et al. 2003](#)). Overall, the outer EBL receives much less attention than the surface layer. This is largely due to the great importance of the surface layer, which governs the air–land, air–sea, or air–ice interaction

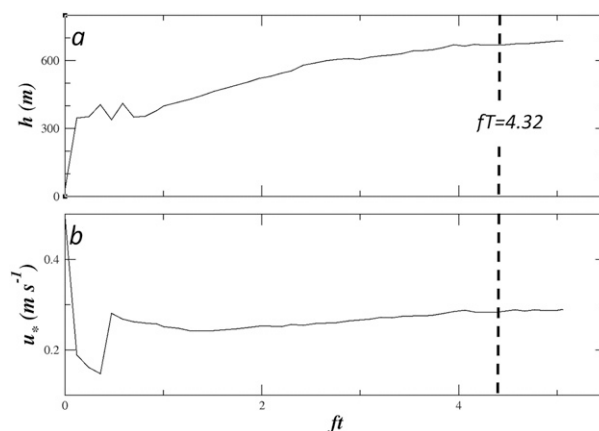


FIG. 2. The variation of the domain-averaged BL (a) height  $h$  (m) and (b) surface friction velocity  $u_*$  ( $\text{m s}^{-1}$ ) with the non-dimensional time  $ft$  derived from the C1 simulations in group C (Table 3). The time corresponding to  $t = 12 \text{ h}$  is indicated (dashed line).

processes, and is most relevant to our daily life. Practically, there are much fewer traditional observations of the outer EBL, which is beyond the range of most meteorological towers. Also, unlike the surface layer, which is predominantly influenced by surface processes, there is additional complexity in an outer layer associated with the impact from surface processes, Earth’s rotation, and boundary layer (BL) top entrainment.

The objective of this study is to advance our understanding of the vertical wind variation in a neutral Ekman boundary layer, including both the surface layer and the outer EBL, using LESs. Particularly, the existence and implications of an elevated log-law layer, located above the surface layer (Fig. 1), are investigated. Besides the scientific merit, there are emerging demands for better understanding of the EBL winds beyond the surface layer. One such example is modern offshore wind turbines, which have hub heights and rotor diameters exceeding 100 m. Therefore, an accurate prediction of winds well above the surface layer is crucial for the wind turbine output power assessment ([Jiang et al. 2008](#)).

The remainder of this paper is organized as follows. The LES code and model configuration are described in section 2. The results from the LESs are presented in section 3. Section 4 contains a derivation of an analytical model that predicts both the lower and upper log-law layers. The results and discoveries are summarized in section 5.

## 2. Model configuration

In the large-eddy simulation code used in this study, the three-dimensional Boussinesq equations (e.g., [Moeng 1984](#); [Sullivan et al. 2014](#)) are integrated forward using a

TABLE 1. Control and derived parameters for group A simulations with  $U_g = 5 \text{ m s}^{-1}$ ,  $z_0 = 0.002 \text{ m}$ , and  $f = 10^{-4} \text{ s}^{-1}$ . The columns 2–9 correspond to the horizontal grid spacing; the first vertical grid spacing; friction velocity at the surface; SGS buffer layer depth; constant-flux layer depth; von Kármán constant derived from the wind speed profile; ratio of the derived and specified surface roughness length; 10-m wind speed; and  $\Delta\hat{W}_{10} = 100(1 - U_{10}/U_{10M})$ , where  $U_{10M}$  is computed using the log law from  $u_*$  and  $z_0$ .

Expt	$\Delta_h$ (m)	$\Delta z_{\min}$ (m)	$u_*$ ( $\text{m s}^{-1}$ )	$Z_b$ (m)	$Z_{\text{cflx}}$ (m)	$\kappa_{\text{LES}}$	$z_{10}/z_0$	$U_{10}$ ( $\text{m s}^{-1}$ )	$\Delta\hat{W}_{10}$ (%)
A1	16	2	0.150	35	28	0.371	3.4	3.72	4.9
A2	8	2	0.147	21	24	0.390	1.7	3.78	2.6
A3	8	1	0.148	20	27	0.395	1.3	3.79	4.3
A4	4	1	0.149	9	24	0.399	1.0	3.89	3.1
A5	2	1	0.146	5	26	0.400	1.0	3.95	<0.1

third-order Runge–Kutta scheme. The equations are discretized with a pseudospectral method in the horizontal coordinates (i.e.,  $x$  and  $y$ ) and a second-order finite-difference scheme in the vertical coordinate (i.e.,  $z$ ), with an SGS model outlined by Moeng and Wyngaard (1988). A further description of the numerical details of this model can be found in Sullivan et al. (2014). For the simulations presented in this study, there are  $256 \times 256$  grid points in the horizontal directions with periodic boundary conditions applied along the lateral boundaries and 160 grid points in the vertical direction. The horizontal grid spacing  $\Delta_h$  varies between 2 and 16 m in group A simulations and is 4 m in the rest. The model top is located at 1950 m, where a radiation boundary condition is applied (Klemp and Durran 1983). The minimal grid spacing is  $\Delta z_1 = 1 \text{ m}$  at the first model level, and the vertical grid spacing increases gradually with altitude following  $\Delta z_{i+1}/\Delta z_i = \gamma$ , where  $i$  is the vertical model level index and  $\gamma \approx 1.03$  is a constant stretching factor. The model is initialized with a unidirectional vertically uniform wind  $\mathbf{V}(z) = (U_g, 0)$ , where the geostrophic wind speed  $U_g$  is 5 or  $10 \text{ m s}^{-1}$ . The free atmosphere is in geostrophic balance with a constant Coriolis parameter  $f = 10^{-4}$  or  $2 \times 10^{-4} \text{ s}^{-1}$ . The atmosphere is neutrally stratified (i.e.,  $d\theta/dz = 0$ ) throughout the domain, and there is no sensible heat flux at the surface. The use of a neutral atmosphere has the advantage of avoiding additional complexity associated with the negative buoyancy flux in the upper portion of the BL, which introduces additional control parameters. This simplification allows us to minimize the number of control parameters to three (i.e., surface

roughness length, geostrophic wind speed, and the Coriolis parameter) and to focus on the characteristics of a rotational shear boundary layer. Additional simulations have been carried out to test the sensitivity of the characteristics of the simulated EBL to the domain size with  $512 \times 512$  horizontal grid points (i.e.,  $2.048 \times 2.048 \text{ km}^2$ ) and a deeper domain (i.e., 3 km with the number of vertical model levels increased to 256). We find that the turbulence statistics and the simulated mean profiles exhibit little sensitivity to the domain size changes (not shown).

The surface stress is computed by applying the similarity theory to the first model level with a specified surface roughness length  $z_0$  which varies from simulation to simulation. The model time step is limited by the Courant–Friedrichs–Lewy (CFL) condition, and the CFL number is calculated from the ratio between the horizontal (vertical) grid spacing and the maximum horizontal (vertical) wind speed. The proper time step can be calculated for a given maximum CFL number, which is set to be 0.3 for this study, that is,  $\max(U\Delta t/\Delta_h, V\Delta t/\Delta_h, w\Delta t/\Delta z) = 0.3$ , where  $\Delta_h$  and  $\Delta z$  denote the horizontal and vertical grid spacings, respectively. The resulting time step  $\Delta t$  varies with the model grid spacings and wind speed.

For each simulation the model is integrated to  $t = 12 \text{ h}$ , corresponding to the nondimensional time  $\hat{T} = ft = 4.32$  and  $8.64$  for  $f = 10^{-4}$  and  $2 \times 10^{-4} \text{ s}^{-1}$ , respectively. Inspection of the temporal evolution of domain-averaged variables such as the surface stress, boundary layer height, and vertically integrated turbulence kinetic energy (not shown) indicates that variations in these domain-averaged

TABLE 2. Control and derived parameters for group B simulations with  $U_g = 5 \text{ m s}^{-1}$  and  $f = 10^{-4} \text{ s}^{-1}$ . The columns 2–9 correspond to the surface roughness length, surface friction velocity, BL height, BL height proportionality coefficient  $C_1 = fh/u_*$ , constant-flux layer depth, von Kármán constant derived from the wind speed profile, ratio between the model derived and specified surface roughness length, slope ratio between the upper and lower log-law layers, and intercept constant for the ULLL.

Expt	$z_0$ (m)	$u_*$ ( $\text{m s}^{-1}$ )	$h$ (m)	$C_1$	$Z_{\text{cflx}}$ (m)	$\kappa_{\text{LES}}$	$z_{10}/z_0$	$\beta$	$z_{20}$ (m)
B1	$2 \times 10^{-4}$	0.149	502	0.36	36	0.400	1.2	1.29	0.0028
B2	$2 \times 10^{-3}$	0.178	620	0.34	39	0.405	1.1	1.38	0.02
B3	$2 \times 10^{-2}$	0.205	665	0.32	42	0.401	0.8	1.30	0.14
B4	0.1	0.231	697	0.30	46	0.398	0.6	1.52	0.68

TABLE 3. Control and derived parameters for group C simulations with  $U_g = 10 \text{ m s}^{-1}$ ;  $f = 10^{-4} \text{ s}^{-1}$ ; and  $z_0 = 2 \times 10^{-4}, 2 \times 10^{-3}, 0.02$ , and  $0.1 \text{ m}$ . The listed parameters are identical to those in Table 2.

Expt	$z_0$ (m)	$u_*$ ( $\text{m s}^{-1}$ )	$h$ (m)	$C_1$	$Z_{\text{cflx}}$ (m)	$\kappa_{\text{LES}}$	$z_{10}/z_0$	$\beta$	$z_{20}$ (m)
C1	$2 \times 10^{-4}$	0.283	670	0.24	52	0.403	0.85	1.54	0.022
C2	$2 \times 10^{-3}$	0.331	700	0.21	68	0.401	1	1.72	0.24
C3	$2 \times 10^{-2}$	0.392	835	0.21	90	0.392	1	1.62	1.0
C4	0.1	0.425	1025	0.24	98	0.402	0.6	1.72	3.0

variables with time become very slow by 12 h, much slower than those in the first 4 h (Fig. 2), suggesting that a quasi-equilibrium Ekman boundary layer has been established. It is noteworthy that, strictly speaking, the BL is not in equilibrium, as the horizontal winds in the BL still rotate slowly associated with inertial oscillations [e.g., Fig. 3 in Andren et al. (1994)], the damping of which may take multiple inertial periods (inertial period  $T_i = 2\pi/f \sim 17.5 \text{ h}$ , for  $f = 10^{-4} \text{ s}^{-1}$ ). On the other hand, for  $ft > 2$ , neither the surface stress nor the BL height exhibits any noticeable oscillation (Fig. 2), suggesting that the impact of inertial oscillations on the BL height, surface-layer characteristics, and the vertically integrated BL turbulence kinetic energy (not shown) is negligible. Unless otherwise noted, the mean profiles presented in this study are averaged horizontally across the model domain and over the last hour (i.e., between 11 and 12 h).

### 3. Results

Four groups of simulations have been carried out to explore the characteristics of the Ekman boundary layer over a range of control parameters (i.e.,  $U_g$ ,  $f$ , and  $z_0$ ). The geostrophic wind is oriented along the  $x$  direction (i.e.,  $G = U_g$  and  $V_g = 0$ ). The model configuration and the control parameters are listed in Tables 1–4, and the results are summarized in sections 3a–c.

#### a. Sensitivity of simulated Ekman boundary layer to the model resolution

A number of simulations have been performed to examine the sensitivity of the simulated EBL to the model horizontal and vertical grid spacings as well as the domain size. The results from a group of five simulations (i.e., group A) are presented here with an emphasis on

the model skill in reproducing the well-established logarithmic wind profiles (i.e., log law) in the surface layer, and the simulated von Kármán constant. The control parameters for group A simulations are  $U_g = 5 \text{ m s}^{-1}$ ,  $f = 10^{-4} \text{ s}^{-1}$ , and  $z_0 = 2 \times 10^{-4} \text{ m}$ . The model grid spacings vary from simulation to simulation (Table 1). Some parameters derived from the group A simulations are listed in Table 1, and the results are summarized in Figs. 3–5.

It is evident that these simulations capture the salient features of a typical Ekman BL, such as Ekman spirals (i.e., the clockwise rotation of the wind direction with height), strong vertical shear in the surface layer, and a supergeostrophic jet in the upper portion of the boundary layer (Fig. 3). The supergeostrophic jet becomes consistently lower and stronger with the decrease of the horizontal grid spacing  $\Delta_h$ . The resolved turbulence kinetic energy (TKE) is characterized by a maximum in the surface layer and a rapid decrease with height aloft (Fig. 3c). In general the TKE maximum becomes systematically larger and exhibits faster decay with height in the simulation with a finer horizontal grid spacing. We define the top of the EBL as the level where the TKE reduces to 5% of its maximum near the surface. The derived BL depth decreases substantially as the horizontal grid spacing  $\Delta_h$  decreases from 16 (i.e., A1) to 4 m (i.e., A4). The decrease of the BL depth is much less pronounced from A4 to A5 (i.e.,  $\Delta_h$  decreases from 4 to 2 m), implying that the simulated BL depth tends to converge as the model horizontal grid spacing consistently decreases.

The mean wind speed and momentum flux profiles are shown in Fig. 4 with the vertical distance from the surface  $z$  in a logarithmic scale. Between approximately 20 and 80 m, the wind speed increases nearly linearly

TABLE 4. Control and derived parameters for group D simulations with  $U_g = 5 \text{ m s}^{-1}$ ;  $f = 2 \times 10^{-4}$ ;  $z_0 = 2 \times 10^{-4}, 2 \times 10^{-3}, 0.02$ , and  $0.1 \text{ m}$ . The listed parameters are identical to those in Table 2.

Expt	$z_0$ (m)	$u_*$ ( $\text{m s}^{-1}$ )	$h$ (m)	$C_1$	$Z_{\text{cflx}}$ (m)	$\kappa_{\text{LES}}$	$z_{10}/z_0$	$\beta$	$z_{20}$ (m)
D1	$2 \times 10^{-4}$	0.148	338	0.46	17	0.147	0.9	0.99	$6 \times 10^{-6}$
D2	$2 \times 10^{-3}$	0.175	385	0.44	20	0.170	0.7	0.95	0.014
D3	$2 \times 10^{-2}$	0.206	420	0.41	26	0.207	0.8	1.19	0.049
D4	0.1	0.234	500	0.43	32	0.234	0.6	1.23	0.21

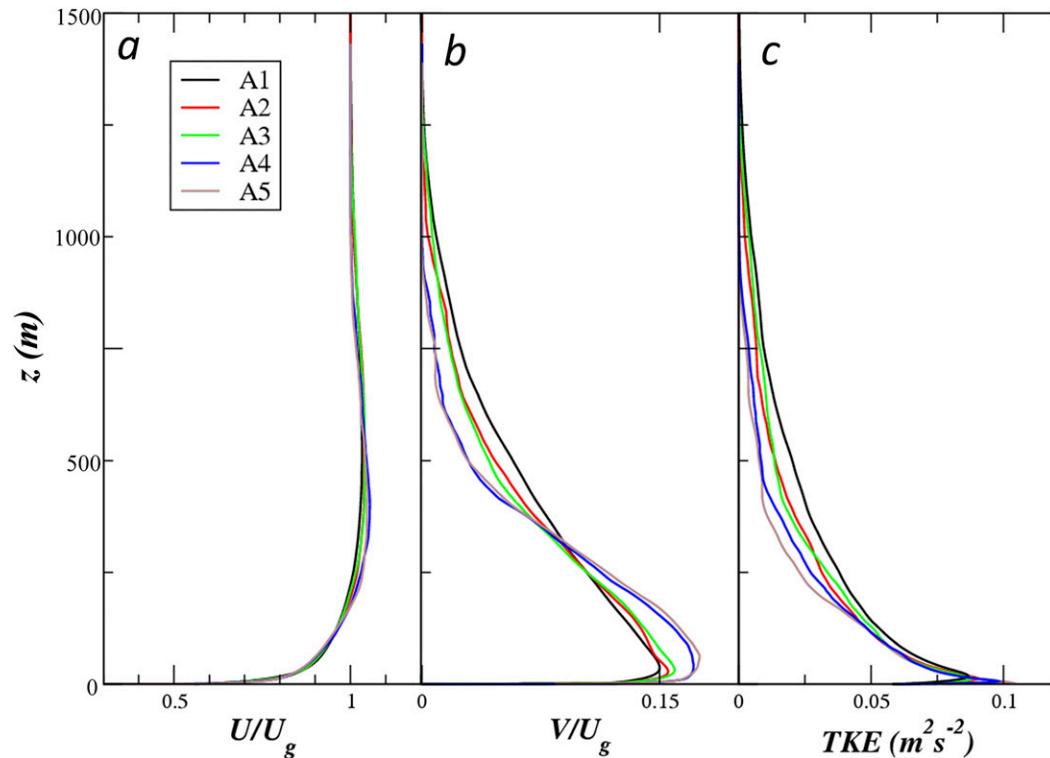


FIG. 3. (a),(b) The horizontal wind components (i.e.,  $U$  and  $V$ ) and (c) the resolved TKE profiles derived from the group A simulations (i.e., A1–A5) are shown as a function of the vertical distance  $z$  for the lowest 1500 m. The horizontal wind components in (a) and (b) are normalized by the geostrophic wind speed.

with  $\log(z)$  (Fig. 4a, the segment indicated by the bold line), suggesting the existence of a log-law layer below 80 m. The total  $x$  momentum fluxes (i.e., sum of the resolved and SGS fluxes) normalized by their corresponding surface stresses are shown in Fig. 4b with the normalized SGS fluxes (dashed curves) included for comparison. The total flux profiles exhibit little discrepancy between simulations. Regardless of the model grid spacings, there appears to be a nearly constant-flux layer in all the simulations. If one defines the depth of the constant-flux layer  $Z_{\text{cflx}}$  as the depth over which the total momentum flux variation is less than 10% (Glickman 2000), then we have  $Z_{\text{cflx}} = 26 \pm 2$  m for the simulations in group A, which is relatively insensitive to the model grid spacing. As expected the parameterized (i.e., SGS) flux dominates near the surface and decreases sharply with the vertical distance from the surface. As the model horizontal grid spacing decreases from 16 to 4 m, the SGS fraction of the momentum flux decreases substantially (e.g., near the bottom, the SGS contribution decreases from 85% for A1 to 45% for A5), implying that a larger percentage of turbulence is resolved around the first model level. The fraction of the SGS flux decreases

faster with the vertical distance from the surface in simulations with finer horizontal grid spacings. We define an SGS buffer layer as the layer where the SGS flux accounts for 10% or more in the total flux (Cai and Steyn 1996), above which energy-containing eddies are considered to be properly resolved. The depth of the SGS buffer layer  $Z_b$  estimated from the group A simulations is listed in Table 1. As expected the SGS buffer layer consistently becomes thinner as the horizontal resolution increases and is relatively insensitive to the variation in vertical grid spacings (comparing A2 and A3). Near the surface the characteristic size of the energetic eddies scales with the vertical distance from the surface  $z$  (Prandtl 1925). According to the Nyquist theorem, the model grid spacing should be at least less than half the characteristic length to be resolved, that is,  $Z_b > 2\Delta_h$ . More generally, we can write  $Z_b = \chi\Delta_h$ , and the constant coefficient  $\chi$  is likely dependent on the SGS model. For example,  $\chi = 3$  is used in Senocak et al. (2007). For this group of simulations, the SGS buffer layer depth is approximately proportional to the horizontal grid spacing with  $\chi \approx 2.5$ .

We are more interested in the mean profiles above the SGS buffer layer, where the turbulence is explicitly



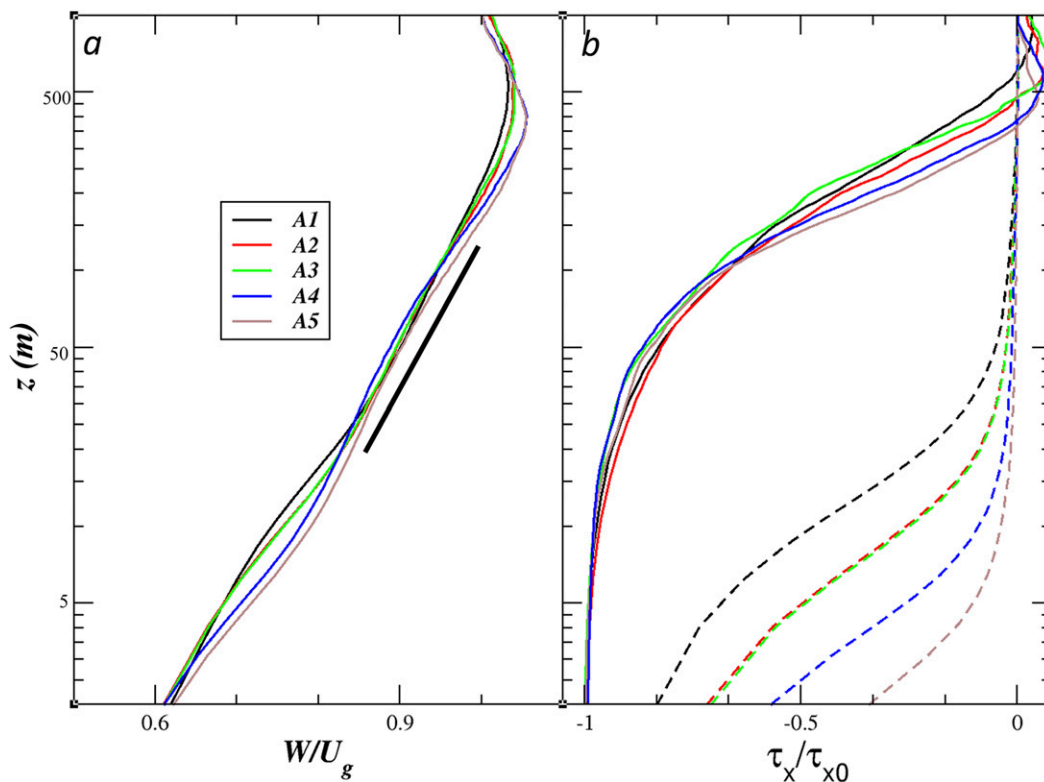


FIG. 4. (a) The normalized wind speed (i.e.,  $W = \sqrt{U^2 + V^2}$ ) and (b) the total momentum flux in the  $x$  direction (i.e.,  $\tau_x$ ) derived from the group A simulations vs the vertical distance  $z$ . The wind speed is normalized by  $U_g$ , and the momentum flux is normalized by the corresponding surface stress in the  $x$  direction  $\tau_{x0}$ . The vertical axis is shown in a logarithmic scale. In (a) the approximate range of the log-law layer is indicated (bold line), and the corresponding SGS contributions are included in (b) as dashed curves.

resolved by the LES code. Specifically, we seek answers to the following questions: 1) Is this LES code capable of producing a log-law layer above the SGS buffer layer? 2) If it is, can the logarithmic profile be used to retrieve the surface friction velocity or von Kármán constant? 3) Is the surface roughness length retrieved from the log-law fitting (i.e.,  $z_{10}$ , referred to as the effective surface roughness length) consistent with the specified value?

Inspection of the mean wind profiles indicates that there exists a well-defined logarithmic layer approximately between  $Z_b$ , the top of the SGS buffer layer, and  $\sim 80$  m above the surface (i.e., the top of the lower log-law layer, denoted as  $Z_{LL}$ ). It is noteworthy that the log-law layer is substantially deeper than the constant-flux layer, which is consistent with the scaling argument in Blackadar and Tennekes (1968) and Tennekes (1973). Next, we perform the linear regression between the wind speed  $W = \sqrt{U^2 + V^2}$  and  $\ln(z)$  using the data points at each model level between  $Z_b$  and  $Z_{LL}$  for every simulation in group A. While the SGS buffer layer top  $Z_b$  can be conveniently determined from the momentum flux profiles, the choice of  $Z_{LL}$  is less straightforward

without the benefit of any guidance from existing studies. Here  $Z_{LL}$  is estimated using a trial-and-error approach, based on the assumption that the wind speed at the model levels within the log-law layer is better linearly correlated with smaller standard deviations. Specifically, we start with a first-guess  $Z_{LL}$  based on visual inspection of the semilogarithmic wind profile and perform linear regression for the segment between  $Z_b$  and  $Z_{LL}$ . We increase the upper limit for the regression range (i.e.,  $Z_{LL}$ ) gradually until the  $t$  value for the slope from the linear regression falls under the threshold value of 100. The obtained  $Z_{LL}$  is rounded to the nearest 10 m. It is worth noting that the threshold  $t$  value used in this study is rather large and that the coefficient of determination (i.e., square of the correlation coefficient) for the linear regression is larger than 0.99 (i.e., the linear regression accounts for more than 99% of the variances).

The wind speed in the log-law layer can be written as  $W = s \ln(z/z_{10})$ , where the slope of the best-fit line and the intercept with  $W = 0$  correspond to  $s = u_* / \kappa_{LES}$  and  $z_{10}$ , respectively. Here  $\kappa_{LES}$  and  $z_{10}$  denote the von

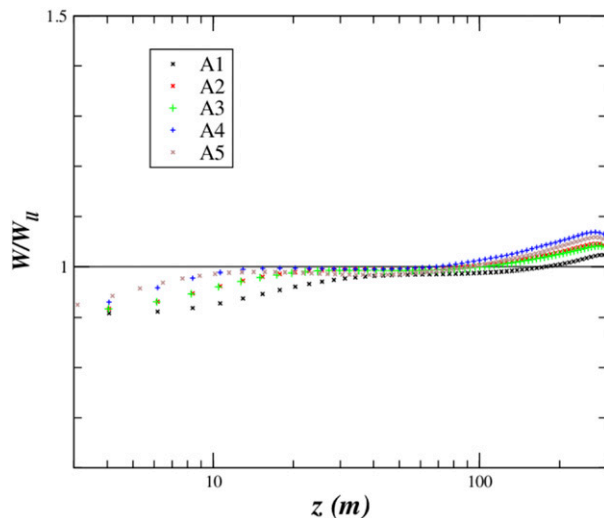


FIG. 5. The normalized wind speed is plotted vs the vertical distance  $z$  for group A. The wind speed is normalized by the logarithmic wind speed  $W_{LL} = (u_*/\kappa) \ln(z/z_{10})$ , and the horizontal axis is plotted on a logarithmic scale.

Kármán constant and effective surface roughness length derived from the linear fitting, respectively. The wind speed  $W$  is used as an approximation of the wind component along the surface stress direction, as the change in the wind direction in the surface layer is usually negligible. The two parameters,  $\kappa_{LES}$  and  $z_{10}$ , obtained from the linear regression are listed in Table 1 for the simulations in group A. For A1, the simulated von Kármán constant is noticeably smaller than 0.4, and the effective surface roughness length is larger than the specified one. As the model resolution increases,  $\kappa_{LES}$  converges toward 0.4 and  $z_{10}$  decreases correspondingly toward  $z_0$ , the specified surface roughness length. For A5, the simulation with the finest grid spacing, we have  $\kappa_{LES} \approx 0.4$  and  $z_{10} \approx z_0$ . Also included in Table 1 is the percentage difference between the 10-m wind speed from the LES run and its counterpart derived from log law using  $u_*$ ,  $\kappa$ , and  $z_0$ . It is evident that the 10-m wind speed predicted by the log law is stronger than that derived from the corresponding LES. The difference is less than 10%, and it consistently decreases with the increase in the model resolution (Table 1). The existence of the SGS buffer and log-law layers is also evident in Fig. 5, which shows the wind speed normalized by the corresponding log-law prediction, that is,  $W/W_{LL}$  as a function of the vertical distance  $z$ . Here  $W_{LL} = (u_*/\kappa) \ln(z/z_{10})$  is computed using the surface friction velocity and the derived surface roughness length. Near the surface (i.e., in the SGS buffer layer), the simulated wind speed is weaker than the log-law prediction with the largest discrepancy occurring at the surface. The log-law layer manifests itself

as the layer between  $Z_b$  and  $\sim 80$  m, where the normalized wind speed is nearly constant (Fig. 5).

In summary, the group A simulations produce all the salient features of a typical Ekman boundary layer, including an Ekman wind spiral, a constant-flux layer, and a well-defined log-law layer located above the SGS buffer layer. In the SGS buffer layer, the energetic eddies are underresolved by the LES code and, consequently, the wind speed deviates from the log law. The depth of the SGS buffer layer decreases linearly with the decreasing horizontal grid spacing, approximately as  $Z_b = 2.5\Delta_h$ . With the increase of the model resolution, the simulated von Kármán constant converges toward 0.4, while the derived surface roughness length tends toward its specified value.

These simulations show that the LES code has difficulty in correctly simulating the vertical gradient of the horizontal winds in the SGS buffer layer, a notorious problem that has been discussed in previous studies. They also demonstrate that when the model grid spacing is fine enough, even though there exists a thin SGS buffer layer where the simulated wind profile deviates from the log law, the LES code is capable of producing a well-defined log-law layer above the buffer layer with the von Kármán constant derived from the best-fit line close to 0.4 and a surface roughness length comparable to the specified one. In other words, these simulations suggest that as the SGS buffer layer becomes thinner, the impact of the wind speed errors in the SGS buffer layer on the interior wind profile becomes consistently smaller. Specifically, the model grid spacing  $\Delta_h = 4$  m and  $\Delta_{z1} = 1$  m appear to be adequate for our study of the neutral Ekman layer. This pair of spacings yields an SGS buffer layer less than 10 m and a von Kármán constant close to 0.4, while the computational cost is acceptable.

#### b. The lower log-law layer and surface layer

Three additional groups of simulations (i.e., B, C, and D) have been carried out with the model configuration identical to that in A4 (i.e.,  $\Delta_h = 4$  m,  $\Delta_{z1} = 1$  m, and the vertical stretching factor  $\gamma \approx 1.03$ ) but different control parameters (i.e., geostrophic wind speed  $U_g$ , Coriolis parameter  $f$ , or surface roughness length  $z_0$ ). The objectives of these simulations are threefold. First, we intend to further evaluate the skill of the LES code in reproducing the log-law wind profile in the surface layer over a broader parameter space. Second, we intend to explore the characteristics of the EBL and their dependence on the three external control parameters. Furthermore, we are interested in characterizing the wind profile beyond the surface log-law layer, and the last objective is addressed in section 3c.

Group B includes four simulations with  $U_g = 5 \text{ m s}^{-1}$ ,  $f = 10^{-4} \text{ s}^{-1}$ , and  $z_0 = 2 \times 10^{-4}, 2 \times 10^{-3}, 2 \times 10^{-2}$ , and



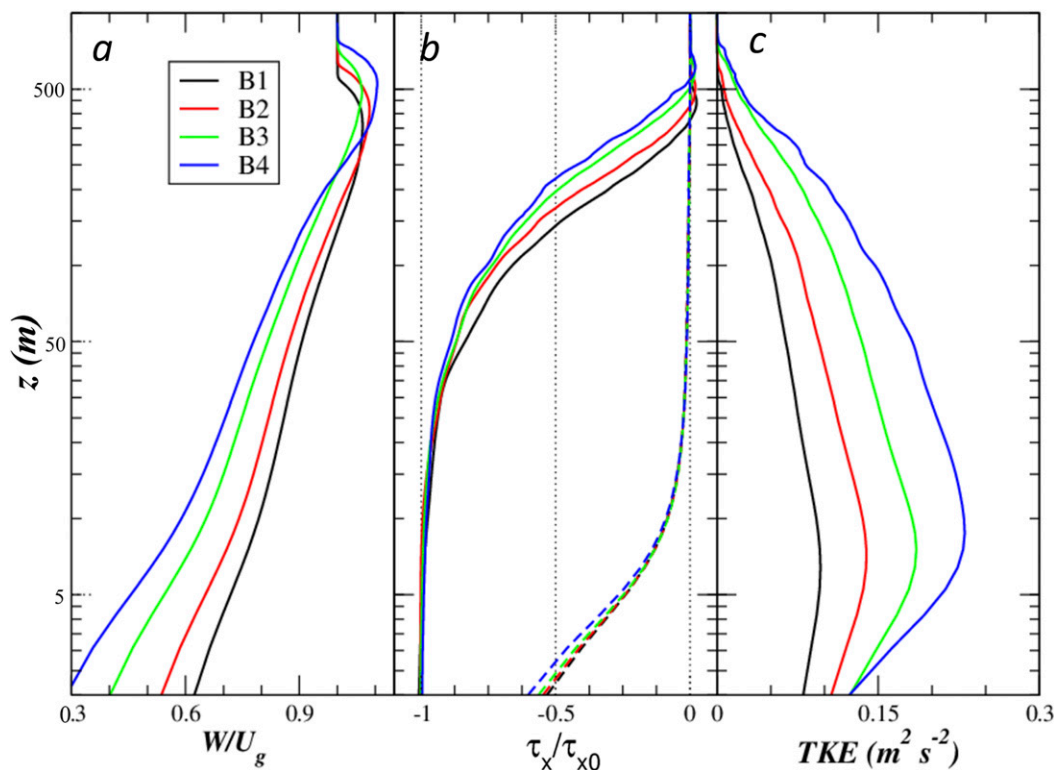


FIG. 6. Profiles of (a) the wind speed normalized by the geostrophic wind speed, (b) the  $x$  momentum fluxes normalized by the surface stress (corresponding SGS components are shown as dashed curves), and (c) TKE ( $\text{m}^2 \text{s}^{-2}$ ), derived from group B simulations, are plotted vs the vertical distance  $z$ . The vertical axis is shown on a logarithmic scale.

0.1 m, respectively; and the results are summarized in Figs. 6 and 7 and Table 2. As expected, over a rougher surface the wind speed near the surface is slower, resulting in stronger vertical wind shear and therefore more intense turbulence (Figs. 6a–c). In accordance with stronger turbulence over a rougher surface, the BL becomes deeper and the supergeostrophic wind maximum becomes progressively stronger. The depth of an Ekman boundary layer  $h$  is often scaled as  $u_* / f$  (Stull 1988) or is written as  $h = C_1 u_* / |f|$ , where the proportionality coefficient  $C_1$  suggested by previous studies ranges between 0.15 and 0.4 (Rossby and Montgomery 1935; Zilitinkevich 1972; Howroyd and Slawson 1975; Panofsky and Dutton 1984). It is worth noting that the BL depth may vary with the BL top definition as well. In this study we define the BL top as the level where the TKE reduces to 5% of its maximum value. Similarly, the BL top can be defined based on potential temperature, wind speed, or momentum flux profiles.

The  $C_1$  values derived from group B simulations decrease from 0.36 for B1 (i.e.,  $z_0 = 2 \times 10^{-4}$  m) to 0.30 for B4 ( $z_0 = 0.1$  m), which is a moderate ( $\sim 12\%$ ) decrease, while  $z_0$  increases by nearly three orders of magnitude.

The normalized SGS momentum flux profiles appear to be rather insensitive to the surface roughness. The SGS buffer layer depth is less than 10 m and shows little change from simulation to simulation. In the meantime, the constant-flux layer depth increases substantially (Table 2). The wind profiles between  $Z_b$  and approximately  $Z_{LL} = 80$  m are virtually linear in the log-linear plots of the wind speed for all the simulations (Fig. 7), indicative of the existence of a logarithmic layer in the simulated wind profiles. For each simulation, a pair of  $z_{10}$  and  $u_* / \kappa_{LES}$  have been derived from the linear regression using data points between  $Z_b$  and  $Z_{LL}$ , where  $Z_b \approx 12$  m is used here, which corresponds to the model level immediately above the actual SGS buffer layer. The estimated upper limit of the log-law layer (i.e.,  $Z_{LL}$ ) using the same trial and error method is around 80 m and tends to increase slowly with the surface roughness length. For simplicity, linear regressions of the wind profiles between  $Z_b = 12$  m and  $Z_{LL} = 80$  m are performed for the simulations in group B (Fig. 7). The corresponding  $\kappa_{LES}$  and  $z_{10}$  values derived from the linear regression are listed in Table 2. A few aspects of the results in Table 2 are worth mentioning. First, the

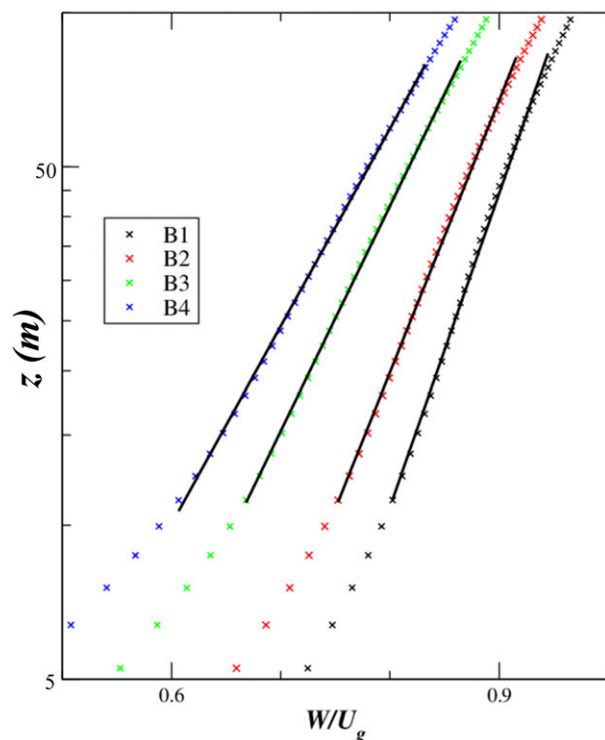


FIG. 7. The normalized wind speed profiles from group B simulations are shown for  $z$  between 5 and 100 m. The vertical axis is on a logarithmic scale. Each symbol corresponds to a vertical model grid point, and the bold lines represent linear regressions over the lower log-law layer.

simulated von Kármán constant  $\kappa_{LES}$  is equal to 0.4, accurate to the second decimal place for all the simulations. Second, the corresponding surface roughness length  $z_{10}$  is close to the specified  $z_0$ . The difference becomes larger for  $z_0 = 0.1$  m, which is likely due to the relatively small ratio between the first model level and the roughness length [i.e.,  $\Delta z_1/z_0 = 10$ ;  $\Delta z_1/z_0 > 50$  recommended by Basu and Lacser (2017)]. Furthermore, while the logarithmic (or log-law) layer is substantially deeper than the constant-flux layer, it is relatively insensitive to the increase in the surface roughness length.

Group C includes four simulations (i.e., C1–C4) identical to the simulations B1–B4 except that the geostrophic wind speed is doubled (i.e.,  $U_g = 10 \text{ m s}^{-1}$ ). The SGS buffer layer depths are comparable to those derived from group B, suggesting that  $Z_b$  is relatively insensitive to the surface roughness length and the geostrophic wind speed. Well-defined log-law layers (Fig. 8a) and constant-flux layers (Fig. 8b) are evident in these simulations. In general, the BL is substantially deeper with much stronger turbulence (Fig. 8c) in these simulations than in their counterpart in group B. The von Kármán constant obtained from the linear fitting of

the wind speed profiles is close to 0.4 as in group B simulations. On the other hand, several discrepancies between groups B and C are worth noting. First, while the BL is deeper in group C, the BL depth proportionality coefficient  $C_1$  values are consistently smaller than their counterparts with a slower geostrophic wind speed (Table 3). The average value of  $C_1$  is 0.25 for group C (i.e., compared to 0.33 in group B) and tends to decrease with increasing surface roughness length. Second, the constant-flux layers are substantially deeper than those in group B but less than doubling. The log-law layer depths for group C are around 110 m, which is about 40% deeper than in group B (Fig. 9).

Simulations in group D are identical to those in group B except that the Coriolis parameter is doubled. The use of  $f = 2 \times 10^{-4} \text{ s}^{-1}$ , which is sizably larger than the Coriolis parameter at the North Pole ( $\sim 1.45 \times 10^{-4} \text{ s}^{-1}$ ), is meant to explore the dependence of the EBL characteristics on  $f$  over a broader range. Again, the SGS buffer layer depth is relatively insensitive to the Coriolis parameter (Figs. 10 and 11; Table 4), and the surface friction velocity is comparable with its counterpart in group B. The increase in the Coriolis parameter leads to a shallower BL with a reduced supergeostrophic wind maximum in the upper BL (Fig. 10a). The proportionality coefficient of the boundary layer depth  $C_1$  is around 0.43, which is substantially larger than those derived from groups B and C. In addition, the constant-flux layer becomes significantly shallower than its counterpart in group B (Fig. 10b) with the TKE maximum in the surface layer comparable to its counterpart in group B (Fig. 10c). A log-law layer is evident in each of the four simulations roughly between  $Z_b \sim 12$  m and  $Z_{LL} \sim 50$  m (Fig. 11), implying that the log-law layer depth is thinner than that in group B.

In summary, over the range of parameters examined, the LES code is able to produce a well-defined surface log-law layer in the mean wind profile. The characteristics of the log-law layer vary with all three control parameters. The derived von Kármán constant is approximately 0.4 and exhibits little variation from simulation to simulation. The depths of the BL and constant flux layer vary with the surface roughness length, geostrophic wind speed, and Coriolis parameter. In Fig. 12, the simulated BL and constant-flux layer depths are plotted versus the characteristic vertical scale  $u_* / |f|$ . While the BL depths for all three groups appear to consistently increase with  $u_* / |f|$ , the proportional coefficient clearly tends to decrease with the increase in  $u_* / |f|$ . Particularly, the proportional coefficient (i.e.,  $C_1$ ) changes from around 0.2 for the simulations with stronger wind speed (i.e., group C) to nearly 0.5 for the simulations with weaker wind speed and a larger

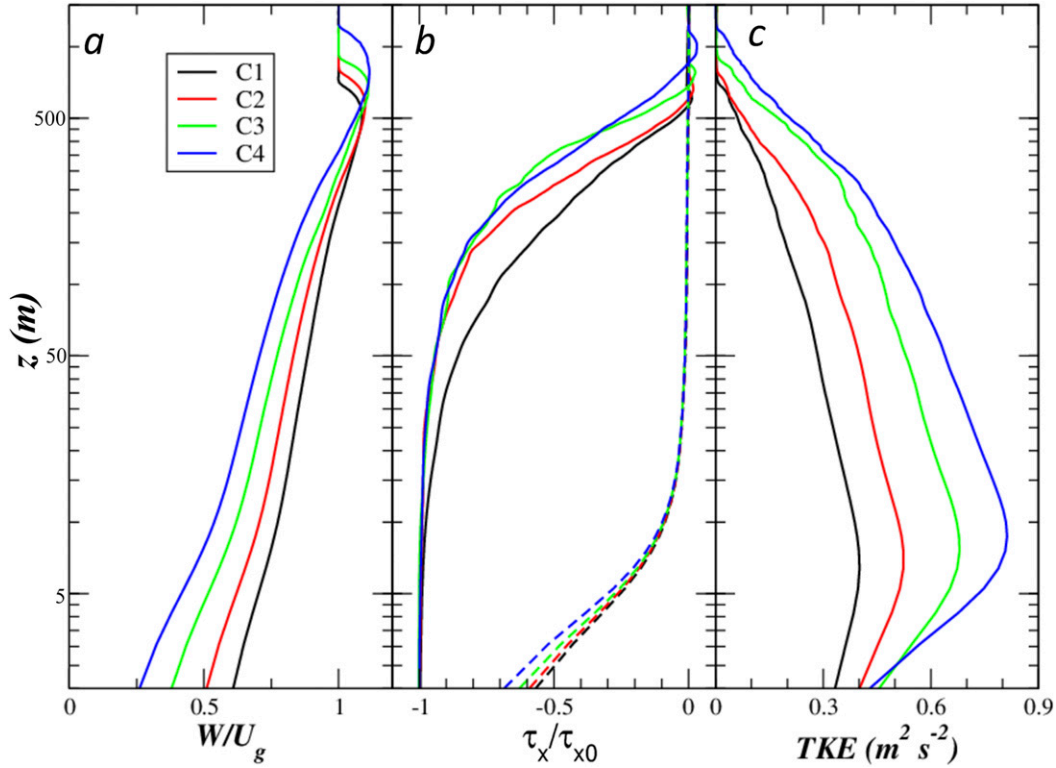


FIG. 8. As in Fig. 6, but for group C simulations.

Coriolis parameter (i.e., group D). On the other hand, the constant-flux layer depth  $Z_{\text{cflx}}$  appears to linearly increase with  $u_* / |f|$  and the linear regression yields

$$Z_{\text{cflx}} = 0.0367 u_* / |f|. \quad (7)$$

In general, the log-law layer becomes deeper under a stronger geostrophic wind speed and shallower over a higher latitude area. Higher towers observed deep log-law layers up to 150 m under neutral atmospheric conditions (Thuillier and Lappe 1964; Carl et al. 1973) and the documented deep log-law layers usually occurred with moderately strong winds, in qualitative agreement with our simulations.

### c. The upper log-law layer

Compared to the surface layer, the wind profile in the outer Ekman BL (referred to the portion above the surface log-law layer here) receives much less attention. A careful diagnosis of the wind profiles from our LESs suggests that there exists a second logarithmic layer, located between the top of the lower log-law layer and the midboundary layer [referred to as the upper log-law layer (ULLL)]. The segment of the wind profiles corresponding to the upper log-law layers for groups B–D is

shown in Fig. 13 along with the linear regression lines. The bottom of the layer is chosen to be the level above the top of the lower log-law layer, and the top of the ULLL is derived using the same trial and error approach as for obtaining  $Z_{\text{LL}}$ . The depth of the upper log-law layer tends to increase with geostrophic wind speed and decrease with the Coriolis parameter.

Similar to the lower log-law layer, the wind speed for the upper log-law layer can be written as  $W_{\text{UL}} = (u_{2*}/\kappa) \ln(z/z_{20})$  and, accordingly, the characteristic velocity  $u_{2*}$  and the length scale  $z_{20}$  can be derived from the linear regression of the mean wind speed over the ULLL segment. The “slope” ratio between the upper and lower log-law layers  $\beta = u_{2*}/u_*$  and  $z_{20}$  are listed in Tables 1–4. The ULLL has the following characteristics. First, the ULLL is found in all the simulations, with its depth comparable to that of the corresponding lower log-law layer. Second, the  $\beta$  value obtained from linear regression is between 0.95 and 1.7 and varies with all three external parameters. Specifically,  $\beta$  appears to be larger over a rougher surface and under stronger geostrophic winds and smaller for a larger Coriolis parameter. For both groups B and C,  $\beta$  is greater than unity and is close to or less than unity in group D with the Coriolis parameter doubled. Third, while the ULLL is

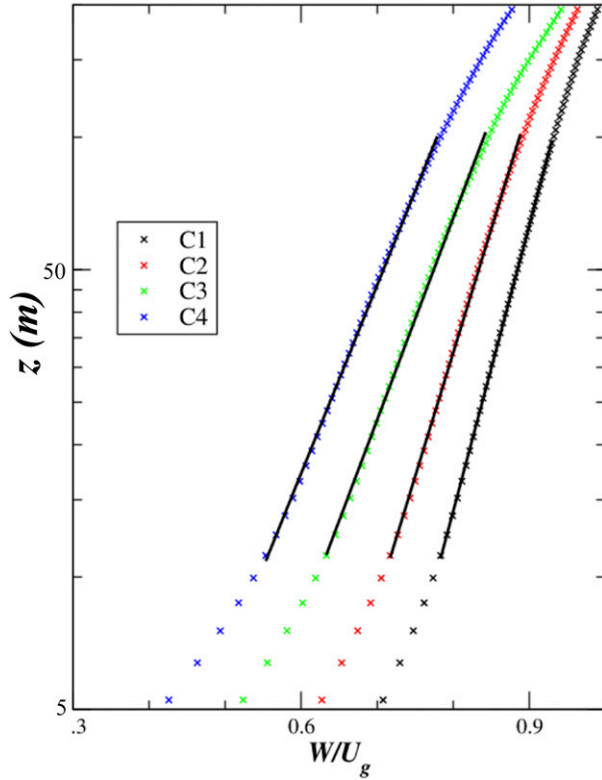


FIG. 9. As in Fig. 7, but for group C with  $z$  between 5 and 200 m.

located almost immediately above the top of the lower log-law layer, presumably there is a thin “buffer” layer between the two (Fig. 1). The wind speed should be a smooth function of the vertical distance (Tennekes 1973). If the two layers are connected, then the slope of the two log-law layers should be the same, which requires  $\beta = 1$  (generally untrue). Further inspection suggests that the variation of  $\beta$  is largely governed by a nondimensional friction velocity  $\hat{u}_* = u_*/(fh)$ , where  $h$  is the BL depth. The  $\beta$  values derived from the three groups of simulations are plotted versus  $\hat{u}_*$  in Fig. 14, which shows that the data points from the three groups of simulations tend to collapse onto a single curve. We further assume that  $\beta = a\hat{u}_*^b$  and that the least squares fitting using the 12 data points from the simulations from groups B–D yields  $\beta = 0.55\hat{u}_*^{3/4}$  (red curve in Fig. 14). Accordingly, the wind profile in the upper log-law layer can be written as

$$W_{UL} = \frac{u_*}{\kappa_2} \left( \frac{u_*}{fh} \right)^{3/4} \ln \left( \frac{z}{z_{20}} \right), \quad (8)$$

where the  $\kappa_2 \approx 1.8\kappa$  is a constant. A few aspects of (8) are worth mentioning. First, (8) suggests that the wind speed in the upper log-law layer is scaled as  $u_*(u_*/fh)^{3/4}$  instead of just  $u_*$ , implying that, as expected, in addition to the

surface stress, the wind speed in the outer Ekman layer is also influenced by Earth’s rotation and the boundary layer depth. Second, assuming the depth of an Ekman BL is given by  $h = C_1 u_*/f$ , where  $C_1$  is a constant, (8) reduces to  $W_{UL} = (u_*/\kappa_3) \ln(z/z_{20})$ , where the new constant  $\kappa_3 = C_1^{3/4} \kappa_2$ . Physically, this implies that the assumption that the proportionality coefficient  $C_1$  is a constant is equivalent to assuming that the wind speed in the outer layer is also scaled as  $u_*$ . Finally, the intercept constant  $z_{20}$  in (8) appears to vary with all three parameters, being more sensitive to  $z_0$  and  $f$  and less so to  $U_g$ . If we assume that the lower and upper log-law layers are nearly adjacent to each other and that the wind speed at the top of the lower log-law layer is approximately equal to that at the bottom of the upper log-law layer, then we have

$$z_{20} = Z_{LL} \left( \frac{z_0}{Z_{LL}} \right)^{1.82(fh/u_*)^{3/4}}. \quad (9)$$

Equation (9) provides a crude estimation of  $z_{20}$  and suggests that  $z_{20}$  is dependent on the surface parameters (i.e.,  $z_0$  and  $u_*$ ), the Coriolis parameter, and the BL depth. The  $z_{20}$  values derived from the three groups of simulations (Tables 2–4) are qualitatively consistent with (9).

#### 4. An analytical EBL model

Unlike the lower log-law layer, to the best of the authors’ knowledge, the upper log-law layer has not been discussed in the literature and is not predicted by any existing theory. Here we attempt to shed some light on the vertical variation of the wind speed in the outer layer by formulating a simple analytical solution for an assumed eddy diffusivity profile.

We start from the  $K$ -theory assumption, that is,

$$\overline{u'w'} = -K_m \frac{\partial U}{\partial z} \quad \text{and} \quad (10)$$

$$\overline{v'w'} = -K_m \frac{\partial V}{\partial z}. \quad (11)$$

Adding the two equations together after multiplying (10) with  $U$  and (11) with  $V$ , we obtain

$$U\overline{u'w'} + V\overline{v'w'} = -WK_m \frac{\partial W}{\partial z}, \quad (12)$$

where  $W = \sqrt{U^2 + V^2}$  denotes the horizontal wind speed. Equation (12) can be written as

$$\tau \cos(\alpha - \alpha_\tau) = -K_m \frac{\partial W}{\partial z}. \quad (13)$$

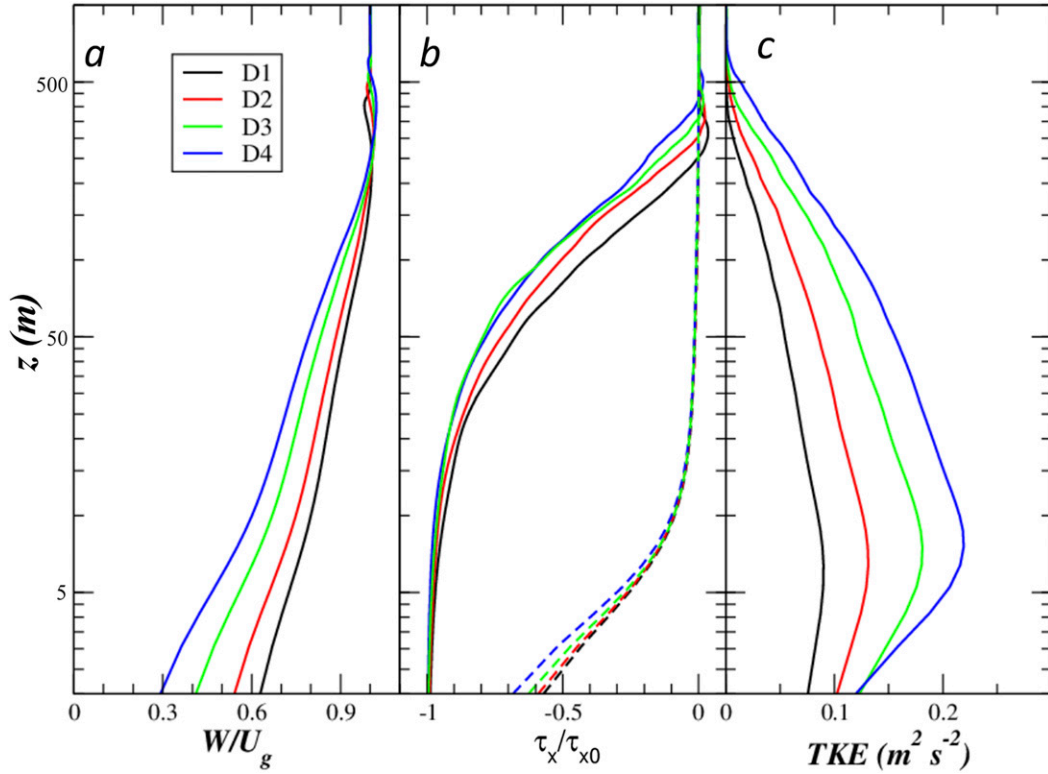


FIG. 10. As in Fig. 6, but for group D simulations.

Here  $\tau = -\sqrt{u'w'^2 + v'w'^2}$  represents the total stress,  $\alpha$  is defined by  $\tan(\alpha) = V/U$ , and  $\alpha_\tau$  is defined by  $\tan(\alpha_\tau) = \overline{u'w'}/\overline{v'w'}$  to denote the wind and stress direction angles (from the  $x$  direction), respectively. Diagnosis of the LESs suggests that the difference in the wind and shear stress directions is relatively small in the lower half of the boundary layer. Hence, we assume that the shear stress is oriented approximately along the wind direction and, consequently, the left-hand side of (13) becomes the total stress. Based on the momentum flux profiles from the LESs, the magnitude of the left-hand side linearly decreases with the altitude in the outer layer, and therefore can be approximated by  $-u_*^2(1 - z/h)$ , where  $h$  represents the BL depth.

We further assume that the eddy diffusivity profile can be approximated by  $K_m = \kappa\lambda u_* z(1 - z/h)$ , where  $\lambda$  is a turbulence-related nondimensional parameter, which varies slowly with the vertical distance  $z$ . Substituting the analytical stress and  $K_m$  expressions into (13), we have

$$\frac{\partial W}{\partial z} = \frac{u_*}{\kappa\lambda z}. \quad (14)$$

If the variation of  $\lambda$  over a vertical distance between any two levels,  $z_1$  and  $z_2$ , is negligible, the wind speed between  $z_1$  and  $z_2$  can be written as

$$W = W_1 + \frac{u_*}{\kappa\lambda} \ln \frac{z}{z_1}, \quad (15)$$

where  $W_1 = W(z_1)$  is the wind speed at the lower reference level  $z_1$ .

In the surface layer, we let  $\lambda = 1$ ,  $z_1 = z_0$ , and  $W_1(z_0) = 0$ , and (15) reduces to

$$W = \frac{u_*}{\kappa} \ln \frac{z}{z_0}, \quad (16)$$

which is almost identical to the well-known log law for the surface layer, except that here  $W$  is the wind speed instead of the wind component along the surface stress direction. This seemingly subtle difference is quite important. The classical theory for the log law assumes that the wind turning across the log-law layer is negligible and that the winds and the shear stress in the log-law layer are oriented along the surface stress direction. The new log law [(16)] allows for a substantial wind turning with altitude as long as the shear stress is approximately oriented along the wind direction at each level throughout the log-law layer. It is also worth noting that the assumed shear stress profile  $\tau = -u_*^2(1 - z/h)$ , is consistent with the traditional constant-flux layer assumption. The depth of a surface (or constant-flux) layer



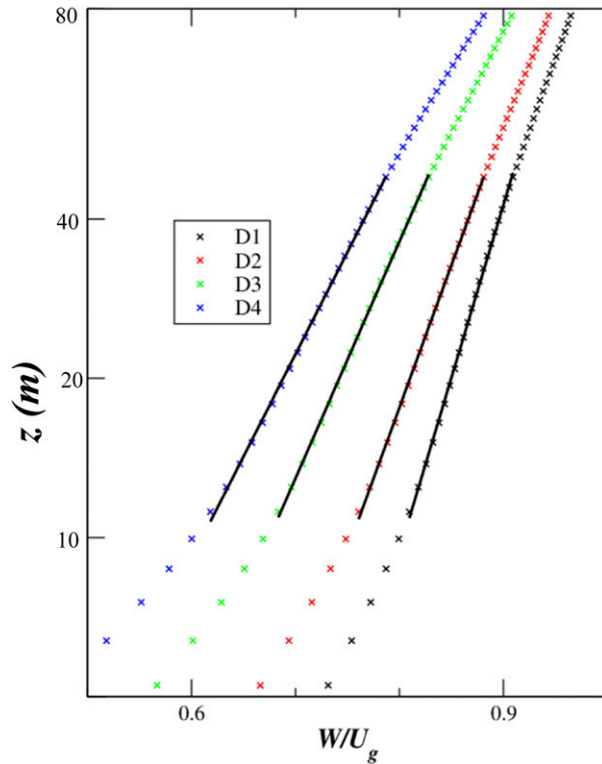


FIG. 11. As in Fig. 7, but for group D with  $z$  between 5 and 80 m.

is around 10% of the BL depth (Glickman 2000), within which the variation of the shear stress is less than 10%. In addition, in the surface layer, where  $z/h \ll 1$ , the assumed  $K_m$  reduces to  $K_m = \kappa \lambda z u_*$ , which is identical to the mixing-length theory assumption (i.e.,  $K_m = \kappa z u_*$ ) for  $\lambda = 1$ .

Similarly, for the upper log-law layer, we rewrite (15) as

$$W = \frac{u_*}{\kappa \lambda} \ln \frac{z}{z_{u0}}, \quad (17)$$

where  $z_{u0}$  is the vertical distance where the best-fit line for the ULLL wind speed intercept  $W = 0$ . The parameter  $\lambda$  in (17) may depart from unity. Comparing (17) with (8) in section 3, we have

$$\lambda = \frac{1}{\beta} = 1.82 \left( \frac{fh}{u_*} \right)^{3/4} \quad (18)$$

for the upper log-law layer. This simple analytical model suggests that the difference in the wind speed scaling for the lower and upper log-law layers is due to the difference in the characteristics of the dominant eddies in the two layers, which leads to the difference in  $\lambda$ , or the eddy diffusivity profile.

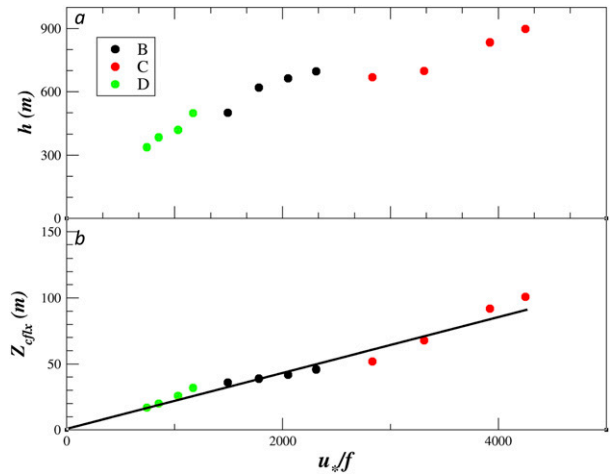


FIG. 12. The depths of (a) the BL  $h$  (m) and (b) the constant-flux layer  $Z_{cflx}$  (m) are plotted vs the length scale  $u_*/f$ . Simulations from groups B, C, and D are shown as black, red, and green dots, respectively. The solid curve in (b) corresponds to the linear regression.

In summary, this simple EBL solution is consistent with the classical mixing-length theory and the log law in the surface layer. It also predicts possible additional log-law layers in the outer layer. However, these solutions are based on strong assumptions about the momentum flux and eddy diffusivity profiles and do not provide any guidance on the adequate vertical distance ranges in which  $\lambda$  can be treated as a constant, which is the necessary condition for (17) to be valid.

## 5. Concluding remarks

The characteristics of wind profiles in an atmospheric Ekman boundary layer have been revisited based on four groups of LESSs. The sensitivity of the simulated wind profiles, especially the characteristics of the classical log-law layer, to the model resolution and domain size are examined utilizing a group of simulations. As the model resolution increases, the SGS buffer layer, the layer where the energetic eddies are underresolved, shrinks. While there is a noticeable deviation from the log law inside the SGS buffer layer in the simulated wind profile, a well-defined log-law layer is evident above the SGS buffer layer. In accordance with the increase in the model resolution, the von Kármán constant derived from the log-law wind profile consistently tends to 0.4, and the effective surface roughness length also converges toward the specified roughness length. This trend is reassuring, as it implies that the impact of the deviation of the wind speed from the log law in the underresolved buffer layer on the interior solution is minimal as long as the model resolution is adequately high.

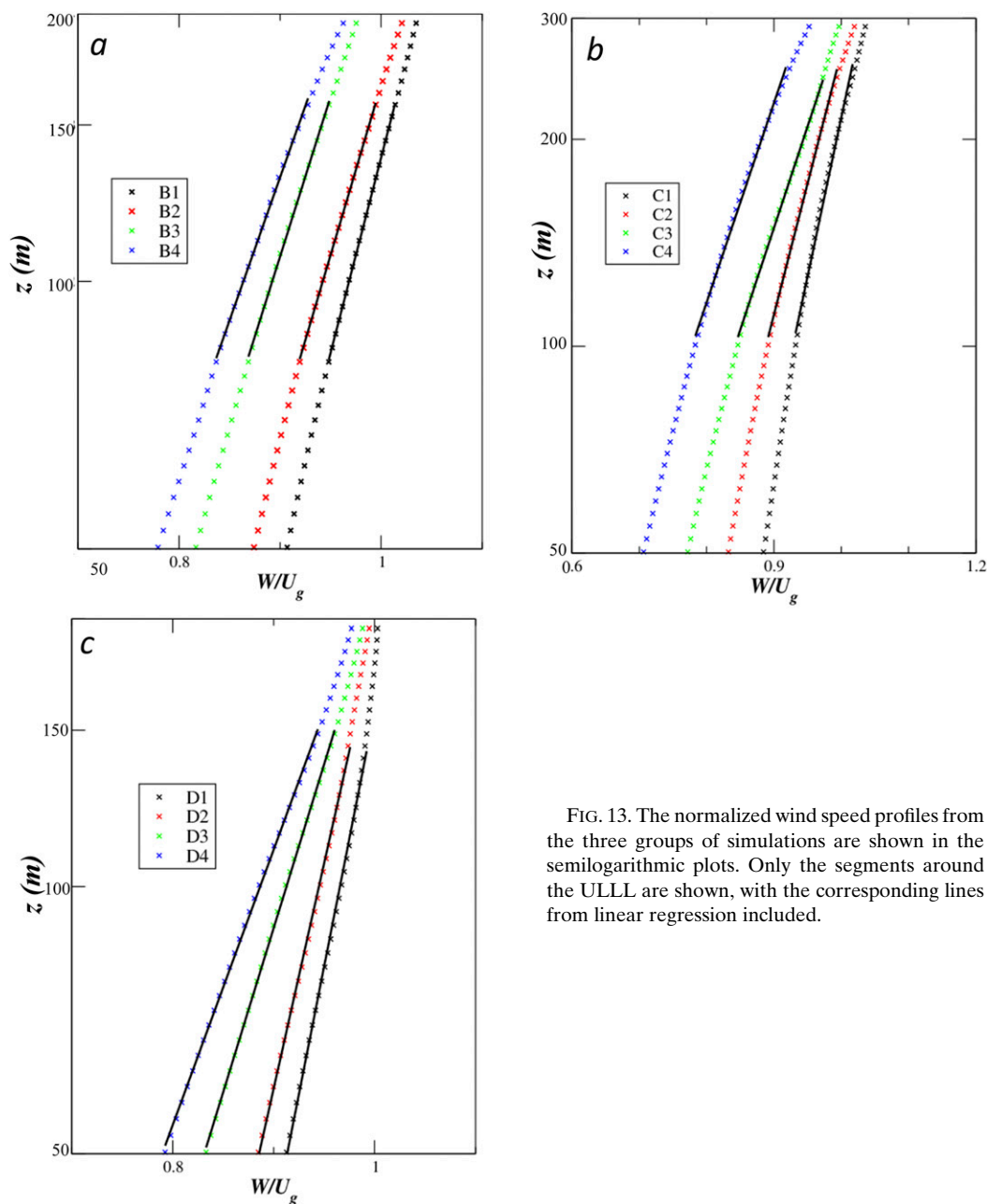


FIG. 13. The normalized wind speed profiles from the three groups of simulations are shown in the semilogarithmic plots. Only the segments around the ULLL are shown, with the corresponding lines from linear regression included.

Three additional groups of simulations have been diagnosed to explore the sensitivity of the wind profiles to three external governing parameters, namely,  $U_g$ ,  $f$ , and  $z_0$ . A constant-flux layer is evident in each simulation with the depth increasing linearly with  $u_* / |f|$  over the parameters examined. The simulated BL depth, defined based on the TKE profile, tends to increase with  $u_* / |f|$  as well, though the proportional coefficient varies with the control parameters instead of being a constant. These simulations also robustly produce wind speed profiles characterized by two separate log-law layers, the canonical log-law layer

above the surface and a second log-law layer located between the lower log-law layer and midboundary layer (Fig. 1). The lower log-law layer is typically deeper than the corresponding constant-flux layer, which is consistent with the prediction by Tennekes (1973) based on a scaling argument. The log-law layer tends to become deeper with stronger geostrophic winds and shallower for a larger Coriolis parameter. In addition to the well-known lower log-law layer, a well-defined elevated log-law layer has been identified from all the simulations with a depth comparable to the lower log-law layer. An analytical

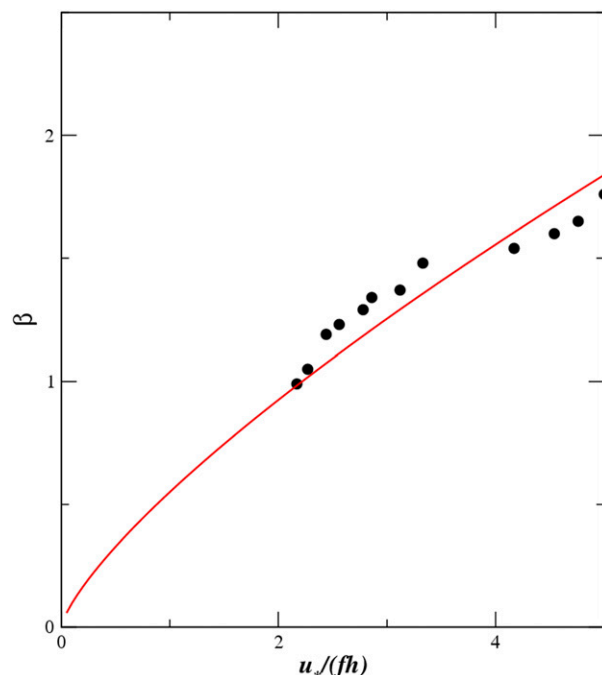


FIG. 14. The  $\beta$  values derived from the three groups of simulations vs the nondimensional friction velocity  $u_*/(fh)$  are shown as black dots. The red curve corresponds to  $\beta = 0.55(u_*/fh)^{3/4}$  and is obtained by a polynomial fit of those data points.

model is examined based on the assumed momentum flux and eddy diffusivity profiles. This model predicts the lower log-law layer above the surface as well as the possibility of log-law layers aloft.

Several aspects of this upper log-law layer are worth noting. First, the wind speed in the two log-law layers appears to have different scaling; the lower layer is scaled with  $u_*$  and the ULLL is scaled with  $u_*(u_*/fh)^{3/4}$ . Physically, this implies that the dominant influence on the lower log-law layer comes from the surface, and other processes, such as the Coriolis effect, are secondary and negligible. The ULLL is influenced by the surface stress and large-scale processes, such as the BL depth and the Coriolis parameter. In the literature there is little discussion of the wind speed scaling for the outer Ekman layer. It has been speculated in Blackadar and Tennekes (1968) that  $u_*(fz_0/u_*)^K$  might be a better scaling for the wind speed in the ULLL than  $u_*$ , where  $K$  is any constant. This scaling may have overemphasized the importance of the surface parameters (i.e.,  $u_*$  and  $z_0$ ) and is inadequate for the parameter space examined in this study. Second, the slope ratio between the upper and lower log-law layers,  $\beta = 0.55(u_*/fh)^{3/4}$ , is typically larger than unity and varies with the geostrophic wind speed, Coriolis parameter, and the BL depth. Under certain conditions—for example, over a higher latitude area—this factor may approach

unity, and the two log-law layers may virtually merge into one deep log-law layer. Third, the upper log-law layer is located almost immediately above the lower log-law layer; however, they are not connected. If the two layers are connected, then both the wind speed and the vertical gradients of the wind speed in the two layers should be equal to each other at the matching (i.e., connecting) level and accordingly  $\beta$  must be unity, which, in general, it is not. Furthermore, the role of the EBL depth plays in the scaling of the outer layer wind speed suggests the importance of the BL depth as an independent parameter for the outer BL, especially in a real atmosphere, where multiple processes are involved in determining the BL depth.

The existence of an upper log-law layer in an Ekman boundary layer has a number of implications. First, if confirmed, the upper log law can be very useful for validating turbulence parameterizations in numerical weather prediction models. Second, from the observational perspective, the upper log-law layer is likely beyond the reach of traditional meteorological towers. However, the wind profile in the outer BL can be observed by remote sensing technologies, such as Doppler lidars and wind profilers as well as instrumented tethered balloons. The findings from this study encourage further investigation of wind profiles beyond the surface layer, especially under nearly neutral conditions. Furthermore, this study hints at the possibility of extending the current similarity theory valid for the surface layer to the midboundary layer.

**Acknowledgments.** This research is supported by the chief of naval research through the NRL Base Program, PE 0601153N. Computational resources were supported by a grant of HPC time from the Department of Defense Major Shared Resource Centers.

## REFERENCES

- Andren, A., A. R. Brown, J. Graf, P. J. Mason, C.-H. Moeng, F. T. M. Nieuwstadt, and U. Schumann, 1994: Large-eddy simulation of a neutrally stratified boundary layer: A comparison of four computer codes. *Quart. J. Roy. Meteor. Soc.*, **120**, 1457–1484, <https://doi.org/10.1002/qj.49712052003>.
- Basu, S., and A. Lacser, 2017: A cautionary note on the use of Monin–Obukhov similarity theory in very high-resolution large-eddy simulations. *Bound.-Layer Meteor.*, **163**, 351–355, <https://doi.org/10.1007/s10546-016-0225-y>.
- Blackadar, A. K., and H. Tennekes, 1968: Asymptotic similarity in neutral barotropic atmospheric boundary layers. *J. Atmos. Sci.*, **25**, 1015–1020, [https://doi.org/10.1175/1520-0469\(1968\)025<1015:ASINBP>2.0.CO;2](https://doi.org/10.1175/1520-0469(1968)025<1015:ASINBP>2.0.CO;2).
- Brasseur, J. G., and T. Wei, 2010: Designing large-eddy simulation of the turbulent boundary layer to capture law-of-the-wall scaling. *Phys. Fluids*, **22**, 021303, <https://doi.org/10.1063/1.3319073>.
- Buschmann, M. H., and M. Gad-el-Hak, 2007: Turbulent boundary layers: Reality and myth. *Int. J. Comput. Sci. Math.*, **1**, 159–176, <https://doi.org/10.1504/IJCSM.2007.016529>.

- Businger, J. A., J. C. Wyngaard, Y. Izumi, and E. F. Bradley, 1971: Flux-profile relationships in the atmospheric surface layer. *J. Atmos. Sci.*, **28**, 181–189, [https://doi.org/10.1175/1520-0469\(1971\)028<0181:FPRITA>2.0.CO;2](https://doi.org/10.1175/1520-0469(1971)028<0181:FPRITA>2.0.CO;2).
- Cai, X.-M., and D. G. Steyn, 1996: The von Kármán constant determined by large eddy simulation. *Bound.-Layer Meteor.*, **78**, 143–164, <https://doi.org/10.1007/BF00122490>.
- Carl, D. M., T. C. Tarbell, and H. A. Panofsky, 1973: Profiles of wind and temperature from towers over homogeneous terrain. *J. Atmos. Sci.*, **30**, 788–794, [https://doi.org/10.1175/1520-0469\(1973\)030<0788:POWATF>2.0.CO;2](https://doi.org/10.1175/1520-0469(1973)030<0788:POWATF>2.0.CO;2).
- Chow, F. K., R. L. Street, M. Xue, and J. H. Ferziger, 2005: Explicit filtering and reconstruction turbulence modeling for large-eddy simulation of neutral boundary layer flow. *J. Atmos. Sci.*, **62**, 2058–2077, <https://doi.org/10.1175/JAS3456.1>.
- Coleman, G. N., 1999: Similarity statistics from a direct numerical simulation of the neutrally stratified planetary boundary layer. *J. Atmos. Sci.*, **56**, 891–900, [https://doi.org/10.1175/1520-0469\(1999\)056<0891:SSFADN>2.0.CO;2](https://doi.org/10.1175/1520-0469(1999)056<0891:SSFADN>2.0.CO;2).
- , J. H. Ferziger, and P. R. Spalart, 1990: A numerical study of the turbulent Ekman layer. *J. Fluid Mech.*, **213**, 313–348, <https://doi.org/10.1017/S0022112090002348>.
- Foken, T., 2006: 50 years of the Monin–Obukhov similarity theory. *Bound.-Layer Meteor.*, **119**, 431–447, <https://doi.org/10.1007/s10546-006-9048-6>.
- George, W. K., and L. Castillo, 1997: Zero-pressure-gradient turbulent boundary layer. *Appl. Mech. Rev.*, **50**, 689–729, <https://doi.org/10.1115/1.3101858>.
- Glickman, T., 2000: *Glossary of Meteorology*. 2nd ed. Amer. Meteor. Soc., 855 pp., <http://glossary.ametsoc.org/>.
- Holton, J. R., 1992: *An Introduction to Dynamic Meteorology*. 3rd ed. Academic Press, 511 pp.
- Horiguchi, M., T. Hayashi, A. Adachi, and S. Onogi, 2012: Large-scale turbulence structures and their contributions to the momentum flux and turbulence in the near-neutral atmospheric boundary layer observed from a 213-m tall meteorological tower. *Bound.-Layer Meteor.*, **144**, 179–198, <https://doi.org/10.1007/s10546-012-9718-5>.
- Howroyd, G. C., and P. R. Slawson, 1975: The characteristics of a laboratory produced turbulent Ekman layer. *Bound.-Layer Meteor.*, **8**, 201–219, <https://doi.org/10.1007/BF00241337>.
- Jiang, Q., J. D. Doyle, T. Haack, M. J. Dvorak, C. L. Archer, and M. Z. Jacobson, 2008: Exploring wind energy potential off the California coast. *Geophys. Res. Lett.*, **35**, L20819, <https://doi.org/10.1029/2008GL034674>.
- Kawai, S., and J. Larsson, 2012: Wall-modeling in large eddy simulation: Length scales, grid resolution, and accuracy. *Phys. Fluids*, **24**, 015105, <https://doi.org/10.1063/1.3678331>.
- Klemp, J., and D. Durran, 1983: An upper boundary condition permitting internal gravity wave radiation in numerical mesoscale models. *Mon. Wea. Rev.*, **111**, 430–444, [https://doi.org/10.1175/1520-0493\(1983\)111<0430:AUBCPI>2.0.CO;2](https://doi.org/10.1175/1520-0493(1983)111<0430:AUBCPI>2.0.CO;2).
- Lee, M., and R. D. Moser, 2015: Direct numerical simulation of turbulent channel flow up to  $Re_\tau \approx 5200$ . *J. Fluid Mech.*, **774**, 395–415, <https://doi.org/10.1017/jfm.2015.268>.
- Mason, P. J., and D. J. Thomson, 1992: Stochastic backscatter in large-eddy simulations of boundary layers. *J. Fluid Mech.*, **242**, 51–78, <https://doi.org/10.1017/S0022112092002271>.
- Millikan, C. B., 1938: A critical discussion of turbulent flows in channels and circular tubes. *Proceedings of the Fifth International Congress for Applied Mechanics*, J. P. Den Hartog and H. Peters, Eds., Wiley, 386–392.
- Moeng, C. H., 1984: A large-eddy-simulation model for the study of planetary boundary-layer turbulence. *J. Atmos. Sci.*, **41**, 2052–2062, [https://doi.org/10.1175/1520-0469\(1984\)041<2052:ALESMF>2.0.CO;2](https://doi.org/10.1175/1520-0469(1984)041<2052:ALESMF>2.0.CO;2).
- , and J. C. Wyngaard, 1988: Spectral analysis of large-eddy simulations of the convective boundary layer. *J. Atmos. Sci.*, **45**, 3573–3587, [https://doi.org/10.1175/1520-0469\(1988\)045<3573:SAOLES>2.0.CO;2](https://doi.org/10.1175/1520-0469(1988)045<3573:SAOLES>2.0.CO;2).
- Monin, A. S., and A. M. Obukhov, 1954: Basic laws of turbulent mixing in the atmosphere near the ground. *Tr. Geofiz. Inst., Akad. Nauk SSSR*, **24**, 163–187.
- Panofsky, H. A., and J. A. Dutton, 1984: *Atmospheric Turbulence: Models and Methods for Engineering Applications*. John Wiley & Sons, 389 pp.
- Prandtl, L., 1925: Bericht über Untersuchungen zur ausgebildeten Turbulenz. *Z. Angew. Math. Mech.*, **5**, 136–139.
- Rossby, C.-G., and R. B. Montgomery, 1935: The layer of frictional influence in wind and ocean currents. Massachusetts Institute of Technology and Woods Hole Oceanographic Institution Papers in Physical Oceanography and Meteorology, Vol. 3, No. 3, 101 pp.
- Senocak, I., A. S. Ackerman, M. P. Kirkpatrick, D. E. Stevens, and N. N. Mansour, 2007: Study of near-surface models for large-eddy simulations of a neutrally stratified atmospheric boundary layer. *Bound.-Layer Meteor.*, **124**, 405–424, <https://doi.org/10.1007/s10546-007-9181-x>.
- Stoll, R., and F. Porté-Agel, 2006: Effect of roughness on surface boundary conditions for large-eddy simulation. *Bound.-Layer Meteor.*, **118**, 169–187, <https://doi.org/10.1007/s10546-005-4735-2>.
- Stull, R., 1988: *An Introduction to Boundary Layer Meteorology*. Kluwer Academic, 666 pp.
- Sullivan, P., J. C. McWilliams, and C. H. Moeng, 1994: A subgrid-scale model for large-eddy simulation of planetary boundary-layer flows. *Bound.-Layer Meteor.*, **71**, 247–276, <https://doi.org/10.1007/BF00713741>.
- , —, and E. G. Patton, 2014: Large-eddy simulation of marine atmospheric boundary layers above a spectrum of moving waves. *J. Atmos. Sci.*, **71**, 4001–4027, <https://doi.org/10.1175/JAS-D-14-0095.1>.
- Tennekes, H., 1973: The logarithmic wind profile. *J. Atmos. Sci.*, **30**, 234–238, [https://doi.org/10.1175/1520-0469\(1973\)030<0234:TLWP>2.0.CO;2](https://doi.org/10.1175/1520-0469(1973)030<0234:TLWP>2.0.CO;2).
- Thuillier, R. H., and U. O. Lappe, 1964: Wind and temperature profile characteristics from observations on a 1400 ft tower. *J. Appl. Meteor.*, **3**, 299–306, [https://doi.org/10.1175/1520-0450\(1964\)003<0299:WATPCF>2.0.CO;2](https://doi.org/10.1175/1520-0450(1964)003<0299:WATPCF>2.0.CO;2).
- von Kármán, T., 1930: Mechanische Ähnlichkeit und Turbulenz. *Nachr. Ges. Wiss. Göttingen. Math.-Phys. Kl.*, **1930**, 58–76.
- Wyngaard, J. C., 2010: *Turbulence in the Atmosphere*. Cambridge University Press, 393 pp.
- , L. J. Peltier, and S. Khanna, 1998: LES in the surface layer: Surface fluxes, scaling, and SGS modeling. *J. Atmos. Sci.*, **55**, 1733–1754, [https://doi.org/10.1175/1520-0469\(1998\)055<1733:LITSLS>2.0.CO;2](https://doi.org/10.1175/1520-0469(1998)055<1733:LITSLS>2.0.CO;2).
- Zikanov, O., D. N. Slinn, and M. R. Dhanak, 2003: Large-eddy simulations of the wind induced turbulent Ekman layer. *J. Fluid Mech.*, **495**, 343–368, <https://doi.org/10.1017/S0022112003006244>.
- Zilitinkevich, S. S., 1972: On the determination of the height of the Ekman boundary layer. *Bound.-Layer Meteor.*, **3**, 141–145, <https://doi.org/10.1007/BF02033914>.